Asynchronous Multiple LiDAR-Inertial Odometry Using Point-Wise Inter-LiDAR Uncertainty Propagation

Minwoo Jung [ID], *Graduate Student Member, IEEE*, Sangwoo Jung [ID], *Graduate Student Member, IEEE*, and Ayoung Kim [ID], *Member, IEEE*

Abstract—**In recent years, multiple Light Detection and Ranging (LiDAR) systems have grown in popularity due to their enhanced accuracy and stability from the increased field of view (FOV). However, integrating multiple LiDARs can be challenging, attributable to temporal and spatial discrepancies. Common practice is to transform points among sensors while requiring strict time synchronization or approximating transformation among sensor frames. Unlike existing methods, we elaborate the inter-sensor transformation using continuous-time (CT) inertial measurement unit (IMU) modeling and derive associated ambiguity as a point-wise uncertainty. This uncertainty, modeled by combining the state covariance with the acquisition time and point range, allows us to alleviate the strict time synchronization and to overcome FOV difference. The proposed method has been validated on both public and our datasets and is compatible with various LiDAR manufacturers and scanning patterns.**

Index Terms—**Range Sensing, SLAM, Mapping.**

I. INTRODUCTION & RELATED WORKS

OVER the last decades, robot navigation using LiDAR has made substantial advances in localization and map construction. Although existing methods mostly solve for a single LiDAR system, limited FOV and occlusion lead to a need for multiple LiDARs. When integrating multiple LiDARs in a complementary configuration, two major challenges impede naive integration, namely temporal and spatial discrepancy.

i) Synchronization: It is straightforward and enticing to secure strict time synchronization among sensors to obtain all measurements at the same time for easy integration. M-LOAM [1] proposed the multiple LiDAR odometry for carefully synchronized LiDAR. In practice, sensors can be synchronized by Pulse per Second (PPS) via external hardware for transmitting the PPS signal. Another option is Precision Time Protocol (PTP), yet not all manufacturers support it, thus requiring sensor combinations made by the same manufacturers.

Due to this sophisticated setting for synchronization, some asynchronous public datasets [2], [3], [4], [5] require software solutions to handle temporal discrepancies. For example, LO-CUS [6] assumed synchronization to merge pointclouds. Later in LOCUS 2.0 [5], they discarded delayed scans for improved robustness accepting induced information loss. Lin et al. [7] applied decentralized Extended Kalman Filter for asynchronous Livox LiDARs; however, their small FOV could induce the error in degenerate environments when processing each LiDAR separately. Nguyen et al. [8] and Wang et al. [9] exploited the IMU to compensate for temporal discrepancies. The idea of utilizing IMU was affordable; still, the error originating from discrete propagation remains. Some researchers suggested using optimization in continuous-time formulation [10], [11]. While this approach can estimate the entire trajectory at any point in time, intensive computational burden hindered real-time feasibility.

In contrast, our method utilizes all available information, including asynchronous scans, and avoiding linear approximation. We decided not to include the continuous term in the optimization phase for a real-time process. Instead, B-Spline interpolation is leveraged to estimate the trajectory for each LiDAR measurement, enabling a computationally efficient solution for multi-LiDAR SLAM in real-world environments.

ii) Spatial Discrepancy: Another solution for this temporal discrepancy is to apply scan matching and compute necessary correction. However, spatial discrepancy induced from different scanning patterns and FOV among LiDARs hinders scan matching in overcoming the temporal discrepancy. Specifically, sparsity and FOV variance from non-repetitive scanning patterns [2] and obliquely installed spinning pattern [3], may yield a little overlapping area among sensors.

iii) Uncertainty Propagation: From both temporal and spatial discrepancy, we inevitably accumulate ambiguity during the projection of the points among sensors. Regarding this issue, proper uncertainty modeling could capture the transferred ambiguity among multiple LiDARs. The usage of uncertainty in LiDAR has been extensively studied in recent years, mostly focusing on learning-based methods [12], [13], [14], [15].

Yet, like ours, some model-based approaches have been presented. For example, Wang et al. [9] calculated the weight for LiDAR residual based on the difference between IMU and LiDAR odometry. Whereas all points were treated equally in [9], we assign point-wise uncertainty by considering their range and

(a) Multi-LiDAR datasets

(b) Constructed map using multi-LiDAR
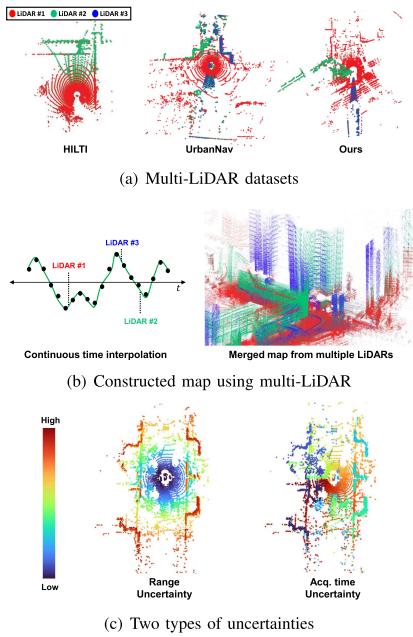

(c) Two types of uncertainties

Fig. 1. (a) Example of FOV difference in multi-LiDAR datasets (b) CT IMU interpolation enable us to merge points accurately, thus substantially increasing net FOV in the accumulated map. (c) Two types of uncertainties considered in this letter.
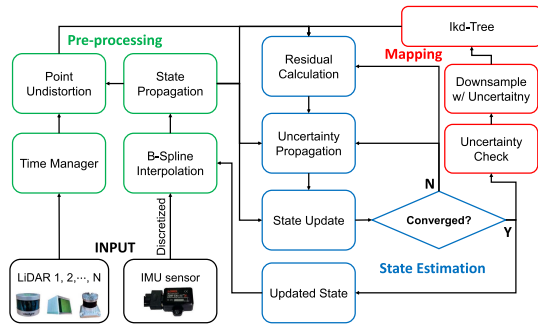

Fig. 2. The proposed method consists of three modules: preprocessing, state estimation, and mapping. In the preprocessing stage, the points from each LiDAR are corrected for distortion and merged by B-spline interpolation. The state estimation stage involves point-wise uncertainty propagation and the application of an IESKF until convergence is achieved. Finally, the optimal state is passed to the IMU model for accurate interpolation in subsequent scans. The data points are projected into ikd-Tree after assessing their uncertainty.

acquisition time. This is particularly important to handle both ambiguities induced by the temporal and spatial discrepancy. M-LOAM [1] propagated the uncertainty in each point by using the extrinsic covariance and the state covariance. This approach is similar to ours in that utilizing state covariance and point-wise uncertainty propagation [16]. Differing from M-LOAM, our method requires no inter-LiDAR overlap for extrinsic covariance update and thus is more generic in handling point-level uncertainty. In [17], authors considered the variance of normal direction using uncertainty to deal with the uneven terrain but without incorporating acquisition time and range ambiguity.

Differing from the existing methods, this letter proposes an asynchronous multiple LiDAR-inertial odometry (Fig. 2). To deal with the abovementioned challenges in multi-LiDAR, we model point-wise uncertainty by considering the range and state covariance at each time. Furthermore, we calculate localization weight using the surrounding environment to determine the

weight term during optimization. Handling a large number of points efficiently, we exploit ikd-Tree [18] and an Iterative Error State Kalman Filter (IESKF), achieving computational efficiency. Our contributions are as follows:

1) We tackle FOV discrepancy by accurately transferring points among LiDARs, which the scan matching approach failed to solve. Furthermore, by utilizing CT B-spline interpolation, we reduce temporal discrepancy, thus yielding consistency in inter-LiDAR scan alignment even with a significant FOV difference.

2) The proposed point-level uncertainty captures increased ambiguity induced by range and point acquisition time. This point-wise assessment assigns larger uncertainty for points farther in range or later in time, hence handling uncertainty more generically.

3) The proposed localization weight balances the ratio between prior and measurement residual during optimization. This enables to automatic adapt the proportion of each residual in degenerate environments such as tunnels and narrow corridors.

4) Our method is validated on public and our own datasets. It is compatible with any combination of LiDAR with different scanning patterns from various manufacturers.

II. METHOD

A. The Notion and State

Subscript A in notation $()_A$ denotes the representing frame. The frame B in frame A is denoted as $()_{AB}$. The ground truth is represented as $()$, while propagated, error, and optimal state are denoted as $\widehat{()}$, $\tilde{()}$, and $\bar{()}$. For simplicity, we classify N LiDARs as $\{L_i, i = 1, \ldots, N\}$, designating the LiDAR with the latest sample point as P and all other LiDARs as S. Our system comprises a state $\mathbf{x}$, input $\mathbf{u}$, and noise $\mathbf{w}$ as

$$\mathcal{M} \triangleq SO(3) \times \mathbb{R}^{15} \times \Pi_{i=1}^{N} \left(SO(3) \times \mathbb{R}^3 \right)$$

$$\mathbf{x} \triangleq \begin{bmatrix} \mathbf{R}_{GI}^T & \mathbf{t}_{GI}^T & \mathbf{v}_{GI}^T & \mathbf{b}_\omega^T & \mathbf{b}_a^T & \mathbf{g}_G^T & \mathbf{R}_{IL_i}^T & \mathbf{t}_{IL_i}^T \end{bmatrix}^T \in \mathcal{M}$$

$$\mathbf{u} \triangleq \begin{bmatrix} \omega_m^T & a_m^T \end{bmatrix}^T, \mathbf{w} \triangleq \begin{bmatrix} n_\omega^T & n_a^T & n_{b\omega}^T & n_{ba}^T \end{bmatrix}^T. \quad (1)$$

For the state $\mathbf{x}$, transformation of the IMU frame (denoted as I) in the global frame (denoted as G) is $\mathbf{T}_{GI} = (\mathbf{R}_{GI}, \mathbf{t}_{GI})$, which consists of the rotation and translation. Additionally, $\mathbf{v}, \mathbf{g}$, and $\mathbf{b}$ stand for velocity, gravity, and bias, while $\mathbf{T}_{IL}$ denote the extrinsic between LiDAR and IMU. $\{\omega_m, a_m\}$ denotes the angular velocity and linear acceleration from IMU sensor. Finally, $\mathbf{w}$ contains the white noise of these variables.

B. IMU Discrete Model With B-Spline Interpolation

The CT kinematic model can be converted into a discrete model using the $\boxplus$ outlined in [18] as

$$\mathbf{x}_{i+1} = \mathbf{x}_i \boxplus \left(\Delta t \mathbf{f} \left(\mathbf{x}_i, \mathbf{u}_i, \mathbf{w}_i \right) \right),$$

$$\mathbf{f}(\mathbf{x}, \mathbf{u}, \mathbf{w}) = \begin{bmatrix} \omega_m - b_\omega - n_\omega \\ \mathbf{v}_{GI} + \frac{1}{2} \left(\mathbf{R}_{GI} \left(a_m - b_a - n_a \right) + \mathbf{g}_G \right) \Delta t \\ \mathbf{R}_{GI} \left(a_m - b_a - n_a \right) + \mathbf{g}_G \\ n_{b\omega} \\ n_{ba} \\ 0_{3\times 1} \\ 0_{3\times 2\tilde{} N} \end{bmatrix}$$

$$(2)$$

merging points obtained at different times into a single frame. This is achieved by determining the relative transformation between frames. Previous studies have utilized approximate discretized IMU or linear interpolation for the inference. Instead, by using B-spline based interpolation, the point p_{Sj} at time t_j can be transformed to the frame at t_l to obtain undistorted point p_{Sj}^u as

$$p_{Sj}^u = \mathbf{T}_{IS}^{-1}{}^B\mathbf{T}_{I^l I^j}\mathbf{T}_{IS}p_{Sj}, \qquad (6)$$

where t_l is the latest arrival time in S, and undistorted point is identified by notation u. Every LiDAR has different arrival times, and the temporal discrepancies should be compensated individually. When merging, the latest arrival time (t_i) of the latest LiDAR (P, denoted as blue point in Fig. 3) is leveraged to transform points acquired by other LiDARs.

$$p_{P^i Sj} = \mathbf{T}_{IP}^{-1}{}^B\mathbf{T}_{I^i I^l}\mathbf{T}_{IS}p_{Sj}^u = \mathbf{T}_{IP}^{-1}{}^B\mathbf{T}_{I^i I^j}\mathbf{T}_{IS}p_{Sj}. \quad (7)$$

This transformation incorporates both undistortion and temporal compensation over multiple frame changes, and errors associated with these changes may be accumulated.

D. Uncertainty Propagation

This uncertainty must be propagated to each point using the covariance to include the errors in the optimization. Covariances of $^B\mathbf{T}$ and $\mathbf{T}_{IL}$ are achieved by (4) and IESKF. Also, the covariance of inverse transformation is calculated through $\Sigma_{inv} = T\Sigma T^T$, where T is the adjoint matrix of $\mathbf{T}^{-1}$. With fourth-order approximation, the transformation and covariance can be combined into $\{\mathbf{T}_{P^i Sj}, \Sigma_{P^i Sj}\}$ [16]. The trace of $\Sigma_{P^i Sj}$ is referred to as the acquisition time uncertainty, which is visualized in Fig. 1.

Three critical improvements beyond previous studies are as follows. Firstly, we distinguish the uncertainty according to the point sampling time, in contrast to assuming the same uncertainty in [1]. Doing so allows a more accurate uncertainty modeling associated with each point. Secondly, the specification of the primary sensor is no longer needed. In [1], because extrinsic covariance is only combined in the secondary LiDAR, the covariance of the secondary LiDAR is always higher than that of the primary LiDAR. Unlike theses, ours is more generic without specifying the primary explicitly. We utilize extrinsic covariances between LiDAR and IMU, resulting in all of the covariances being combined with the extrinsic covariance. This yields the covariances being equally affected by the extrinsic covariance. Finally, in contrast to the [1], which propagates uncertainty in the global frame, our approach propagates uncertainty on a per-point basis by confining it to the LiDAR frame. This decision aimed to account for the uncertainty introduced when fusing individual LiDAR points. By transforming a point into the frame P, the transformed point is presented as

$$p_{P^i Sj} \triangleq \widehat{\mathbf{T}}_{P^i Sj}\widehat{p}_{Sj} = \exp(\xi_{P^i Sj}^\wedge)\mathbf{T}_{P^i Sj}(p_{Sj} + D\zeta)$$
$$\approx (I + \exp(\xi_{P^i Sj}^\wedge))\mathbf{T}_{P^i Sj}(p_{Sj} + D\zeta) \qquad (8)$$

Here, ξ is the error of the transformation and $\zeta \in \mathbb{R}^3$ is the perturbation of the LiDAR measurement. Also, p in (8) is a 4×1 vector with a scale value 1 added, and D is the dilation matrix which transforms the dimension from 3×1 to 4×1, with zero terms added. As the second-order error is computationally expensive but has a relatively small effect, we only consider the
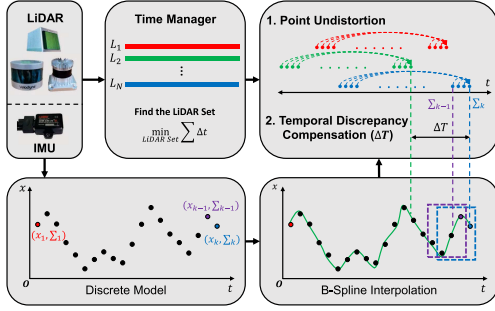

Fig. 3. IMU inputs are propagated by a discrete model and fed into B-spline interpolation. We search the LiDAR that satisfies the minimal time differences. Based on the interpolation, (i) a pointcloud from LiDAR is undistorted by transformed into a single frame (the last point) and (ii) the temporal discrepancy is compensated by the relative transformation among the last points in each LiDAR.

Here, the function $\mathbf{f}$ describes the state of the system to its subsequent state and is parameterized by the discretization interval Δt. During the time interval between $(i-1)$ and $(i)^{\text{th}}$ scans, the system estimates the trajectory using the IMU, assuming the $(i-1)^{\text{th}}$ state to be optimal.

$$\widehat{\mathbf{x}}_{k+1} = \widehat{\mathbf{x}}_k \boxplus (\Delta t\mathbf{f}(\widehat{\mathbf{x}}_k, \mathbf{u}_k, \mathbf{0})); \widehat{\mathbf{x}}_0 = \bar{\mathbf{x}}_{i-1} \qquad (3)$$

$$\widehat{\Sigma}_{k+1} = \mathbf{F}_{\tilde{\mathbf{x}}_k}\widehat{\Sigma}_k\mathbf{F}_{\tilde{\mathbf{x}}_i}^T + \mathbf{F}_{\mathbf{w}_k}\mathbf{Q}_k\mathbf{F}_{\mathbf{w}_i}^T; \widehat{\Sigma}_0 = \bar{\Sigma}_{i-1}, \qquad (4)$$

where $\mathbf{Q}_k$ denotes the covariance of $\mathbf{w}_k$ while the jacobians $\mathbf{F}_{\tilde{\mathbf{x}}_k}$ and $\mathbf{F}_{\mathbf{w}_k}$ represent the derivatives of $(\mathbf{x}_{k+1} \boxminus \widehat{\mathbf{x}}_{k+1})$ with respect to each subscript, under the conditions that $(\tilde{\mathbf{x}}_k, w_k) = (0,0)$. Also, $\widehat{\mathbf{x}}_{k-1}$ can be achieved using the $\boxminus$ operator as detailed in [19]. The accuracy of the interpolation is directly dependent on the accuracy of the discrete model. Since the IMU discrete model before optimization may not be accurate, the IMU state preceding $\bar{\mathbf{x}}_{i-1}$ is recalculated via $\boxminus$ operator.

Based on this propagation, B-spline interpolation is performed utilizing four transformations in the global frame, known as control points from $\mathbf{T}_{GI}^{k-1}$ to $\mathbf{T}_{GI}^{k+2}$ [11]. By this interpolation, the trajectory at any time can be estimated, which is especially beneficial for asynchronous sensor systems. Furthermore, it is highly effective in environments with curved trajectories due to smoothness of spline. The system estimates the transformation at any time $t \in [t_k, t_{k+1})$ using

$$^B\mathbf{T}_{GI}(s(t)) = \mathbf{T}_{GI}^{k-1}\Pi_{n=1}^3 \exp\left(\tilde{\mathbf{B}}_j(s(t))\Omega_{k+n-1}\right), \quad (5)$$

while $t_k = k\Delta t$ with $\Delta t = t_{k+1} - t_k$, and $s(t) = (t - t_k)/\Delta t$. Ω_k denotes the incremental control pose which is calculated as $\Omega_k = \log((\mathbf{T}_{GI}^{k-1})^{-1}\mathbf{T}_{GI}^k)$. $\tilde{\mathbf{B}}_j$ is the matrix that includes the square term of s, and notation $^B\mathbf{T}$ means that it is calculated by B-spline. Lastly, to obtain the covariance calculated in (4), $\widehat{\Sigma}_{k+1}$ is assigned to the transformation achieved at $t \in [t_k, t_{k+1})$. The overall process is illustrated in Fig. 3.

C. Preprocessing of Multi-LiDAR System

Despite the strict interpolation, the interpolated pose accuracy is directly affected by the minimum difference in arrival times among LiDARs. Therefore, a set of LiDAR is chosen to minimize the sum of differences in the arrival times.

For undistortion, we focus on a single LiDAR, S, applying the same process to others. The first step of distortion starts with

first-order term, $\widehat{\mathbf{T}}\widehat{p} \approx \mathbf{q} + \mathbf{Q}\theta$.

$$\mathbf{q} := \mathbf{T}p, \ \mathbf{Q} := \left[(\mathbf{T}p)^{\odot} \ \mathbf{T}D\right], \ \begin{bmatrix} \epsilon \\ \eta \end{bmatrix}^{\odot} := \begin{bmatrix} \eta\mathbf{1} & -\epsilon^{\wedge} \\ \mathbf{0}^T & \mathbf{0}^T \end{bmatrix}$$

$$\theta := \begin{bmatrix} \xi^T & \zeta^T \end{bmatrix}^T, \ \theta \sim \mathscr{N}(\mathbf{0}, \Xi), \ \Xi = \text{diag}(\Sigma_{P^l S^j}, \mathbf{Z}), \quad (9)$$

with the LiDAR measurement covariance $\mathbf{Z}$. Since $p_{P^i S^j}$ follows the Gaussian distribution, the uncertainty of the point can be obtained through (9), as $\Sigma_p = \mathbf{Q}\Xi\mathbf{Q}^T$. The resulting uncertainty is derived from the range of point p from $(\mathbf{T}p)^{\odot}$, and the acquisition time from $\Sigma_{P^l S^j}$. Improved accuracy is achieved by addressing ambiguity from IMU discrete model error over time and noise effects which increase with range from vibration. It is utilized for the optimization with p_{S^j}.

E. Measurement Model With Uncertainty

Our system utilizes a surface measurement model without feature extraction under the assumption of local planarity. The points, $\{\mathbf{p}_{S^j}, j = 1, \ldots, l\}$ in the LiDAR frame can be transformed to the global frame with the following equation:

$$\mathbf{p}_{GS^j} = \mathbf{T}_{GI^i}\mathbf{T}_{IP}\mathbf{p}_{P^iS^j} = \mathbf{T}_{GI^i}{}^B\mathbf{T}_{I^iI^l}\mathbf{T}_{IS}\mathbf{p}^u_{S^j} \quad (10)$$

For the LiDAR P, which sample the point lastly, ${}^B\mathbf{T}^{-1}_{GI^i}{}^B\mathbf{T}_{GI^l}$ is equivalent to the identity matrix as there is no temporal discrepancy to be compensated. To approximate the surface, our method selects the five nearest neighbor points from the measurement in the ikd-Tree. In doing so, our system incorporates the associated uncertainty of points in the ikd-Tree into the measurement model. For generality, we use the notation L, indicating the LiDAR, S or P. The weighted sample covariance of the plane for point p_{L^j}, Σ_{L^j} is calculated as

$$\Sigma_{L^j} = \sum_{n=1}^{5} w_n^2 \Sigma_n, \quad w_n = \frac{\tau - \text{tr}(\Sigma_n)}{\sum_{n=1}^{5}[\tau - \text{tr}(\Sigma_n)]} \quad (11)$$

while τ represents the uncertainty threshold, which is also utilized in the mapping process in the subsequent section. Based on the normal vector of the plane, $\mathbf{v}_{GL^j}$, and the plane covariance, Σ_p, the measurement model is calculated as

$$\mathbf{0} = \mathbf{h}_{L^j}(\mathbf{x}_i, \mathbf{n}_{L^j})$$

$$= \frac{\mathbf{v}^T_{GL^j}\left(\mathbf{T}_{GI^i}{}^B\mathbf{T}_{I^iI^l}\mathbf{T}_{IL}\left(\mathbf{p}^u_{L^j} + \mathbf{n}_{L^j}\right) - \mathbf{q}_{GL^j}\right)}{\text{FIC}\left(\text{tr}(\Sigma_{L^j}), s_{\max}, s_{\min}\right)} \quad (12)$$

Here, $\mathbf{n}_{L^j}$ represents the noise from the LiDAR, and $\mathbf{q}_{GL^j}$ is a point located on the plane. Additionally, $\mathbf{h}$ represents the measurement model, which is summary of the terms of state, including $\mathbf{T}_{GI}$ and $\mathbf{T}_{IL}$. We employ fixed interval conversion (FIC) to bind the uncertainty, which is calculated as

$$\text{FIC}(V, I_{\max}, I_{\min}) = \frac{(I_{\max} - I_{\min})(V - V_{\min})}{V_{\max} - V_{\min}} + I_{\min}, \quad (13)$$

with $I_{\max}$ and $I_{\min}$ to be the rescaling interval. Similarly, $V_{\max}$ and $V_{\min}$ are the maximum and minimum values in V. Utilizing FIC, we balance measurement influence by adjusting the values within set bounds, which regulates performance and reliability without overemphasis or neglect.

F. Iterated Error State Kalman Filter

Our state estimation comprises three components as in Fig. 2, namely state propagation, residual calculation, and state update.

The state propagation component, as represented in (3) and (4), is utilized as the prior distribution, and its error state is obtained through

$$\mathbf{x}_i \boxminus \widehat{\mathbf{x}}_i = (\widehat{\mathbf{x}}_i^{\kappa} \boxplus \tilde{\mathbf{x}}_i^{\kappa}) \boxminus \widehat{\mathbf{x}}_i = \widehat{\mathbf{x}}_i^{\kappa} \boxminus \widehat{\mathbf{x}}_i + \mathbf{J}^{\kappa}\tilde{\mathbf{x}}_i^{\kappa} \sim \mathscr{N}(\mathbf{0}, \widehat{\Sigma}_i). \quad (14)$$

$\mathbf{J}^{\kappa}$ represents the Jacobian matrix of $(\widehat{\mathbf{x}}_i^{\kappa} \boxplus \tilde{\mathbf{x}}_i^{\kappa}) \boxminus \widehat{\mathbf{x}}_i$ with the condition that $\tilde{\mathbf{x}}_i^{\kappa} = 0$. When $\kappa = 1$, $\mathbf{J}^{\kappa} = \mathbf{I}$ and transformation term in $\widehat{\mathbf{x}}_i$ becomes ${}^B\mathbf{T}_{GI^i}$. Further details are as in [19].

In the case of the measurement model, another distribution can be identified through a first-order approximation:

$$\mathbf{0} = \mathbf{h}_{L^j}(\mathbf{x}_i, \mathbf{n}_{L^j}) \simeq \mathbf{h}_{L^j}(\widehat{\mathbf{x}}_i^{\kappa}, \mathbf{0}) + \mathbf{H}^{\kappa}_{L^j}\tilde{\mathbf{x}}_k^{\kappa} + \mathbf{v}_{L^j}$$

$$-\mathbf{v}_j = \mathbf{z}^{\kappa}_{L^j} + \mathbf{H}^{\kappa}_{L^j}\tilde{\mathbf{x}}_k^{\kappa} \sim \mathscr{N}(\mathbf{0}, \Sigma_{L^j}) \quad (15)$$

where $\mathbf{H}^{\kappa}_{L^j}$ is the Jacobian of $\mathbf{h}_{L^j}(\widehat{\mathbf{x}}_i^{\kappa} \boxplus \tilde{\mathbf{x}}_i^{\kappa}, \mathbf{n}_{L^j})$ with $\tilde{\mathbf{x}}_i^{\kappa}$, and $\mathbf{v}_j$ is the noise with covariance calculated as in (9).

Utilizing both prior distribution (14) and measurement distribution (15), the state estimation problem is changed into maximum a posteriori (MAP):

$$\min_{\tilde{\mathbf{x}}_i^{\kappa}} \left(\|\mathbf{x}_i \boxminus \widehat{\mathbf{x}}_i\|^2_{\widehat{\Sigma}_i} + w_l^2 \sum_{L=P,S}\sum_{j=1}^{m} \|\mathbf{z}^{\kappa}_{L^j} + \mathbf{H}^{\kappa}_{L^j}\tilde{\mathbf{x}}_i^{\kappa}\|^2_{\mathbf{R}_{L^j}} \right) \quad (16)$$

while $\mathbf{R}_{L^j}$ is the output from $\text{FIC}(\text{tr}(\Sigma_{L^j}), \mathbf{R}_{\max}, \mathbf{R}_{\min})$, and $\|\mathbf{x}\|^2_{\Sigma} = \mathbf{x}^T\Sigma^{-1}\mathbf{x}$. The localization weight, w_l, is given to the prior distribution over measurement, especially for the degenerated environment. The value of w_l can be determined by taking the ratio of σ_1 to σ_3, which are obtained from Singular Value Decomposition (SVD) of the normal vector of the measurement. If w falls outside of the boundary of $(b_{\min}, b_{\max})$, the values of $l_{\min}$ and $l_{\max}$ are assigned to w_l, respectively. Otherwise, the value of w_l can be obtained as $w_l = \text{FIC}(w, l_{\max}, l_{\min})$. An iterated Kalman filter can solve this maximum a posteriori (MAP) problem.

$$\mathbf{K} = \left(\mathbf{H}^T\mathbf{R}^{-1}\mathbf{H} + \mathbf{P}^{-1}\right)^{-1}\mathbf{H}^T\mathbf{R}^{-1},$$

$$\widehat{\mathbf{x}}_i^{\kappa+1} = \widehat{\mathbf{x}}_i^{\kappa} \boxplus \left(-\mathbf{K}\mathbf{z}_i^{\kappa} - (\mathbf{I} - \mathbf{KH})(\mathbf{J}^{\kappa})^{-1}(\widehat{\mathbf{x}}_i^{\kappa} \boxminus \widehat{\mathbf{x}}_i)\right) \quad (17)$$

with $\mathbf{H} = w_l \times [\mathbf{H}^{\kappa}_{S^1}{}^T, \ldots, \mathbf{H}^{\kappa}_{S^m}{}^T, \mathbf{H}^{\kappa}_{P^1}{}^T, \ldots, \mathbf{H}^{\kappa}_{P^m}{}^T]^T$, $\mathbf{R} = \text{diag}(\mathbf{R}_{S^1}, \ldots, \mathbf{R}_{S^m}, \mathbf{R}_{P^1}, \ldots, \mathbf{R}_{P^m})$, $\mathbf{P} = (\mathbf{J}^{\kappa})^{-1}\widehat{\Sigma}_i(\mathbf{J}^{\kappa})^{-T}$, and $\mathbf{z}_i^{\kappa} = w_l \times [\mathbf{z}^{\kappa}_{S^1}{}^T, \ldots, \mathbf{z}^{\kappa}_{S^m}{}^T, \mathbf{z}^{\kappa}_{P^1}{}^T, \ldots, \mathbf{z}^{\kappa}_{P^m}{}^T]^T$. The iterative process is repeated until the convergence criteria, which $\|\widehat{\mathbf{x}}_i^{\kappa+1} \boxminus \widehat{\mathbf{x}}_i^{\kappa}\| < \epsilon$ is satisfied. The final estimates of the state and its corresponding covariance are as:

$$\bar{\mathbf{x}}_i = \widehat{\mathbf{x}}_i^{\kappa+1}, \quad \bar{\Sigma} = (\mathbf{I} - \mathbf{KH})\mathbf{P} \quad (18)$$

G. Mapping With Uncertainty

Using the estimated state, $\bar{\mathbf{x}}_i$, the pointcloud from LiDAR can be transformed into the global frame,

$$\bar{\mathbf{p}}_{L^j} = \bar{\mathbf{T}}_{GI^i}{}^B\mathbf{T}_{I^iI^l}\bar{\mathbf{T}}_{IL}\mathbf{p}^u_{L^j}. \quad (19)$$

To effectively maintain the ikd-Tree, the uncertainty of the point is first evaluated. If the uncertainty of a point, $\text{tr}(\Sigma_{L^j})$, is larger than a predefined τ, that point is not saved in the tree. The saved points are then added to the tree via downsampling. In contrast to the original ikd-Tree, our proposed strategy considers uncertainty during the insertion process. The downsampling process is designed to retain only points close to the center of

Dataset	Number	LiDAR	IMU	Environment
Hilti	1 2	OS0-64 Livox Horizon	200Hz	Indoor & Outdoor
UrbanNav	1 2 3	HDL-32E VLP-16 LS-16C	400Hz	Urban with Skyscrapper
Ours	1 2 3	OS2-128 Livox Avia Livox Tele	100Hz	Urban with Challenges

the tree resolution for accurate mapping. In our implementation, if the insertion point lies within the diagonal value of $\mathbf{Z}$ at the center of the tree, points with low uncertainty are retained in the tree.

III. EXPERIMENT

A. Dataset and Evaluation

1) Dataset: To evaluate the performance of our method in various environments, we conduct experiments on three datasets: Hilti SLAM Dataset 2021 [2], UrbanNav [3], and our dataset. In the Hilti dataset, we evaluate our method for a hand-held system in small-scale indoor and outdoor environments. The UrbanNav dataset is exploited to assess the performance of a method for a vehicle-like system in an urban environment at a large scale. In addition to public datasets, we collect our dataset to assess the performance in challenging environments at a higher speed ($\sim$50 skm/h) including U-turns and tunnels. To synchronize the temporal foundation of each sensor, PTP was employed. However, this does not imply that all sensors were firing simultaneously. The datasets are listed in Table I, with detailed descriptions of each sequence provided in subsequent sections.

2) Evaluation: Ours is compared with three state-of-the-art methods including Fast-LIO2 (single) [18], M-LOAM (multi) [1], and LOCUS 2.0 (multi) [5]. To ensure the fair comparisons, we employ the following strategies. Fast-LIO2 only supports single LiDAR, and we utilize the central LiDAR as it provides the most points. For the Hilti dataset, we obtain the trajectory from each LiDAR, OS0-64 (denoted as FAST-O) and Livox Horizon (denoted as Fast-H). For M-LOAM, which supports spinning LiDAR, we incorporate the points from Livox LiDAR as a surface feature. For LOCUS 2.0, we readjust the parameters for GICP to adapt to the specific environment. Notably, no odometry input is provided in the dataset. In our method, we select the parameters as $\mathbf{Z} = \mathrm{diag}(0.05, 0.05, 0.05)$, $(s_{\min}, s_{\max}) = (1, 1.25)$, $(b_{\min}, b_{\max}) = (0.2, 0.8)$, $(l_{\min}, l_{\max}) = (0.5, 3)$, $(R_{\min}, R_{\max}) = (0.0075, 0.0125)$ and $\tau = 1$ with little variation.

To quantitatively compare the performance of methods, we calculate the Root Mean Square Error (RMSE) of the absolute trajectory error (ATE) and relative trajectory error (RTE) using Evo evaluator [20]. The ATE is measured in meters and degrees, while the RTE is measured in percentage and degree per meter. For the Hilti dataset, we leverage the evaluator provided by the dataset to calculate the ATE_t, translation component of the ATE. While for our dataset, the ground truth is obtained using an Inertial Navigation System (INS). To ensure the reliability of the results, we only utilize positions with the status, INS_SOLUTION_FREE.

	Ours	Fast-H	Fast-O	M-LOAM	LOCUS 2.0
Basement	**0.036**	0.709	*0.046*	0.115	0.120
Campus	**0.046**	0.063	*0.063*	0.386	0.087
Construct	**0.063**	0.200	*0.088*	2.647	0.290
LAB	**0.024**	Err	*0.026*	0.064	0.040
UZH	**0.177**	0.233	0.184	0.276	*0.177*

The best results are in **bold** and the second-best's are in *italic*.
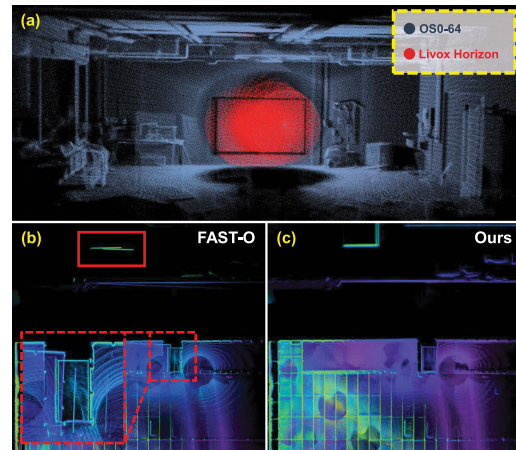

Fig. 4. (a) Accumulated scans from LAB. Compared to Ouster (gray), Livox (red) reveals very limited FOV and causes localization failure due to the lack of distinct features. (b-c) show the outputs of Fast-O and our method for the Parking dataset. As shown in the red box in (b), the map produced by Fast-O is misaligned when returning to the starting point, while our result in (c) is well aligned.

B. Hilti SLAM Dataset 2021

The results from the Hilti evaluator are presented in Table II. Among all methods, ours yields the most accurate results in all sequences. Interestingly, Fast-O achieves the second-best performance in most sequences, even without using multi-LiDAR. As expected, M-LOAM and LOCUS 2.0 are less accurate than the others, attributed to the lack of synchronization of inter LiDAR. In the case of LAB and UZH, the impact of asynchrony is minimal since intense movement does not exist in the indoor environment. However, in the case of Campus and Construct, which involve more vigorous movement, the errors are more pronounced due to the inherent asynchrony of the sensors. Despite these challenges, our method exhibits robustness in all sequences owing to its temporal compensation.

Meanwhile, unlike Fast-O, Fast-H is degenerated significantly due to the limited FOV of the LiDAR. The limited FOV of Livox is prone to encounter degenerate cases as depicted in Fig. 4(a). This FOV-induced limitation may yield a substantial tracking deviation even in the presence of a rich feature. In this perspective, Fast-O seems the best choice for most environments, but it is not optimal in all cases, particularly in the Parking. Since the ground truth of Parking is not provided, we examine the reconstructed map for qualitative evaluation as illustrated in Fig. 4(b). In the center of the Parking, a substantial number of points are not detected, causing a tracking error and drift in the map. On the other hand, our method can mitigate these issues by incorporating additional LiDAR as shown in Fig. 4(c), demonstrating the robustness of the multi-LiDAR system.

TABLE III
UrbanNav Dataset Evaluation

		Fast-LIO2	M-LOAM	LOCUS 2.0	Ours
Mongok	ATE_t	*5.917*	25.899	6.846	**2.579**
	ATE_r	*4.039*	9.140	5.616	**2.383**
	RTE_t	0.188	0.632	*0.174*	**0.167**
	RTE_r	0.749	1.006	**0.710**	*0.736*
Whampoa	ATE_t	*7.066*	31.482	18.124	**4.236**
	ATE_r	*7.066*	8.286	9.404	**4.600**
	RTE_t	0.390	0.710	*0.339*	**0.207**
	RTE_r	*1.034*	1.213	1.238	**1.033**
TST	ATE_t	*8.783*	53.682	33.292	**2.342**
	ATE_r	*6.640*	21.584	13.367	**5.085**
	RTE_t	*0.494*	2.177	0.841	**0.351**
	RTE_r	*1.264*	1.355	1.748	**1.261**

The best results are in **bold** and the second-best's are in *italic*.

TABLE IV
Private Dataset Evaluation

		Fast-LIO2	M-LOAM	LOCUS 2.0	Ours
City01	ATE_t	*9.970*	33.907	23.998	**6.538**
	ATE_r	*4.575*	8.792	5.521	**3.491**
	RTE_t	*0.292*	0.955	0.609	**0.266**
	RTE_r	*0.898*	1.020	0.895	**0.874**
City02	ATE_t	*35.308*	72.382	58.211	**6.707**
	ATE_r	7.473	*4.683*	4.722	**3.522**
	RTE_t	*0.608*	3.665	1.531	**0.565**
	RTE_r	1.179	*1.104*	1.167	**1.084**
City03	ATE_t	*6.951*	33.801	21.753	**5.470**
	ATE_r	*4.194*	6.657	4.773	**3.522**
	RTE_t	0.996	1.310	1.159	**0.565**
	RTE_r	1.088	**1.070**	1.089	*1.084*

The best results are in **bold** and the second-best's are in *italic*.

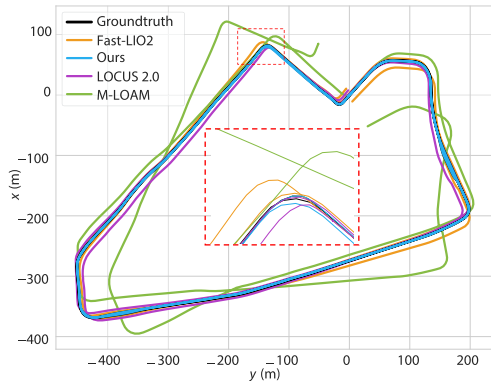Fig. 5.　Trajectory of TST from all methods. Our method (blue) demonstrates a highly close alignment with the ground truth (black).
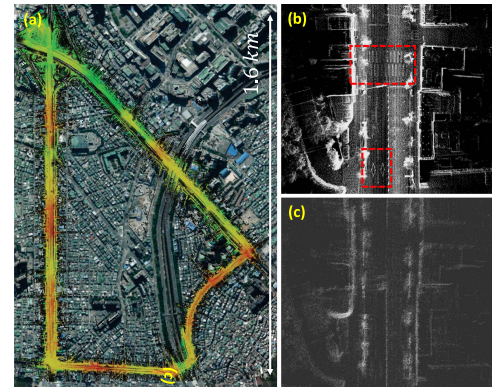

Fig. 6.　(a) The map of City03 features points color-coded by height, with low (red) to high (green) values. On the right, stack scans from (b) our method and (c) LOCUS 2.0 are displayed. Our approach effectively compensates for temporal discrepancies, achieving low noise even with street markers present, as illustrated in the red box.

C. UrbanNav Dataset

The UrbanNav Dataset consists of three spinning LiDARs with two mounted on both sides in an inclined configuration. This configuration maximizes the scanning area but with minimal overlap, and can detect objects at higher elevations that are invisible to the central LiDAR. However, since this dataset contains multiple dynamic objects at a higher driving speed, inter-LiDAR transformation encompasses significant variations due to temporal discrepancies from asynchrony.

As shown in Table III, our method outperforms all others. In the Mongok, most methods show minor errors due to the repeated traversal of a single loop. However, Whampoa exhibits more significant error in most algorithms as there is an underpass in the middle of the trajectory (Fig. 8(b)). Additionally, the higher vehicle speed in the TST—approximately twice that of the Mongok scenario—has exacerbated the error of the multi-LiDAR system due to the difficulties in merging pointclouds in asynchronous systems. Despite these challenges, the proposed method can effectively suppress significant errors by accurately estimating the relative transformation inter-LiDAR and allowing extensive scanning, which is impossible with a single LiDAR (Fig. 5).

D. Our Own Dataset

Our dataset, City01-03, presents a unique set of challenges, whereas our proposed method achieves superior performance in most cases, as presented in Table IV. City01 includes many rotations and U-turns. After completing a U-turn,

both M-LOAM and LOCUS 2.0 experienced localization failure when attempting to match the previously generated map. This failure is attributed to the lack of an initial estimation in LOCUS 2.0 and the inability to align the scans among LiDARs. As a result, the system resorts to constructing an additional map for localization.

City02 features a tunnel environment with a length of approximately 400 m. In this sequence, failure to establish correspondences between points in the tunnel interrupts estimating forward motion yielding a significant error.

Lastly, City03 is over 4.3km with numerous dynamic objects and no loops until the return to the start point with a large accumulated error. Among others, our method exhibits low error in City03, even in the absence of a loop in the middle of the trajectory. For example, the map is well-aligned after completing a single lap as presented in Fig. 6. Despite using asynchronous LiDAR, our method can generate clarified maps with reduced noise thanks to our temporal compensation and accurate odometry.

E. The Effect of B-Spline and Uncertainty Propagation

1) Module-Wise Comparison: Entire algorithm (FULL) consists of B-spline interpolation (CNT) and uncertainty propagation with localization weight (UNC). We test a baseline using an IMU discrete model and uniform weight for all points (denoted

TABLE V
COMPONENT-WISE COMPARISON USING ATE$_t$

	RAW	CNT	F-UNC	UNC	FULL
City01	7.345	7.280	7.001	*6.831*	**6.538**
City02	7.346	*6.835*	7.058	6.844	**6.707**
City03	6.043	5.969	6.547	*5.837*	**5.470**
Mongok	2.652	*2.597*	2.645	2.611	**2.579**
Whampoa	4.728	4.463	4.657	**4.078**	*4.236*
TST	2.721	**2.143**	2.773	2.752	*2.342*

The best results are in **bold** and the second-best's are in *italic*.

as RAW). Additionally, we evaluate a method employing a single state covariance for uncertainty propagation, as in the case of M-LOAM (F-UNC), using the last covariance of the scan for point-wise uncertainty propagation. All of the methods are verified using ATE$_t$.

Table V presents the ATE$_t$ for each test case. Both RAW and CNT address temporal discrepancies utilizing interpolation techniques; however, the CNT demonstrates slight improvement by using B-spline interpolation. This interpolation is particularly effective for datasets that exhibit highly curved trajectory. As expected, the ATE$_t$ is reduced in the UrbanNav dataset, which has a higher IMU frequency (400 Hz) than the our own Dataset (100 Hz). This result demonstrates that temporal compensation and undistortion with B-spline interpolation are effective in both cases, regardless of the IMU frequency. The effect of point-wise uncertainty is the most critical, as can be seen from UNC, while F-UNC shows some level of error reduction but not as much as ours.

In City01-03, FULL yields the best results by effectively harnessing the benefits of both methods. However, the UrbanNav dataset shows varied results due to environmental factors. Stationary and low-speed segments lead to less pronounced effects of B-spline interpolation and point-wise uncertainty, resulting in similar performance in Mongok. In TST, the inclined LiDAR occasionally detects fewer points and becomes the primary LiDAR, leading to lower uncertainty compared to the front LiDAR. Consequently, the performance of UNC slightly declines compared to RAW, which subsequently impacts the results of FULL. Conversely, in Whampoa, increased environmental complexity allows for more effective point-wise uncertainty and localization weight, even when the primary LiDAR changed, resulting in significant performance increase in UNC. Although the competing effect between B-spline interpolation and point-wise uncertainty leads to lower performance in FULL compared to UNC, the error is significantly reduced compared to RAW. In conclusion, both proposed methods generally improves performance when uses individually or in combination.

2) Mapping Capability: A qualitative comparison is given in Fig. 7 when we test RAW and UNC in LAB sequence. Because the small FOV is critically limited in this small indoor environment, this sequence is tricky to localize when equipped only with Livox Horizon. Unlike RAW that fails in consistent mapping, UNC localizes successfully in this confined space. As evidenced by the results in Table V and Fig. 7, we can infer that the uncertainty model plays a leading factor in the enhancement of performance in our method.

3) Localization Weight: In Fig. 8, we depict partial maps of the City02 and Whampoa. The narrow nature of these environments may result in correspondence error, leading to prior residuals having a stronger influence than measurement residuals. As seen in Fig. 8(a) and (b), localization weight is
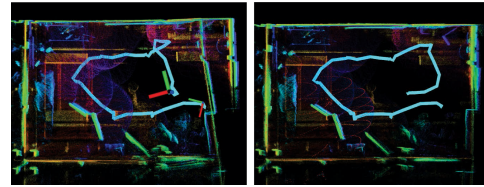
(a) The output of RAW   (b) The output of UNC

Fig. 7. This map is generated using Livox Horizon after the successful initialization (60sec from starting) in the LAB. (a) unsuccessful mapping in this degenerate environment. (b) consistent map by the proposed method overcoming the environment.
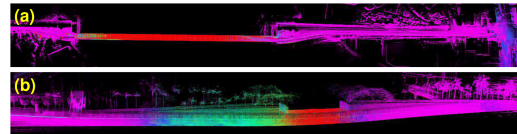

Fig. 8. Partial maps of (a) City02 and (b) Whampoa display points color-coded by localization weight, ranging from low (red) to high (pink). Both maps exhibit an apparent weight decrease in tunnel regions, with (b) showing a less significant decrease due to the upper part of the underpass being open and scanned by inclined LiDAR.
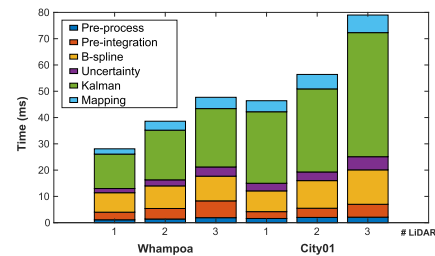

Fig. 9. Computation times with respect to the number of LiDARs. Pre-process is the computation time for reformatting the pointcloud. Pre-integration involves integrating IMU measurements and undistorting the point. B-spline is utilized during undistortion and is separately listed from pre-integration. Uncertainty includes time for calculating the point-wise uncertainty and localization weight.

noticeably reduced only in degenerate surroundings, which is expected and highlights the effectiveness of our localization weight in such challenging environments.

F. The Effect of the Number of LiDAR

1) Time: We analyze the time consumption for Whampoa and City01, which have the most extensive distance among the UrbanNav and our datasets. To assess the real-time performance, we measure the average processing time per scan for each module, as in Fig. 9 and Table VI. During all experiments, downsampling with 0.4 m resolution was implemented. Table VI exhibits the number of points obtained following this operation. As can be seen, our method is light-weight and fully supports real-time performance even for a multi-LiDAR system. One of the modules in our method, uncertainty propagation, can be completed within a maximum of 5 ms, even though it significantly improves performance. In contrast, the B-spline interpolation takes longer because undistortion is done before downsampling. However, even in City01 with many points, our method spends

TABLE VI
TIME ANALYSIS ACCORDING TO THE NUMBER OF LiDAR [MS]. THE
NUMBERING FOLLOWS THE DESCRIPTION IN TABLE I

	Whampoa			City01		
LiDAR #	1	2	3	1	2	3
Point (Down.) #	4045	5647	6784	8554	10172	12244
LiDAR	HDL-32E	+VLP-16	+LS-C16	OS2-128	+Avia	+Tele
Preprocess	1.1	1.4	1.9	1.6	2.0	2.1
Pre-integration	2.9	4	6.4	2.6	3.5	4.9
B-Spline	7.4	8.6	9.4	7.9	10.5	13.1
Uncertainty	1.6	2.3	3.5	2.9	3.3	5
Kalman Filter	13.1	18.9	22.2	27.2	31.6	47.2
Mapping	2.0	3.4	4.3	4.2	5.5	6.7
Total	28.1	38.6	47.7	46.4	56.4	79

*Specification: Intel i7 CPU@2.50Ghz and 48GB RAM

No.	Median ATE_t
1 (RAW)	5.76
1 (FULL)	5.65
2 (RAW)	5.27
2 (FULL)	5.08
3 (RAW)	5.22
3 (FULL)	4.73

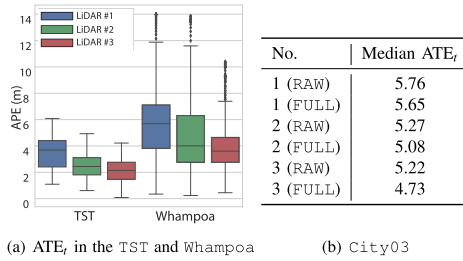(a) ATE_t in the TST and Whampoa   (b) City03

Fig. 10. (a) an evaluation about three cases for two datasets. From left, the median values of ATE_t and standard deviations are: (3.69, 1.22), (*2.44*, **0.96**), (**2.14**, *0.98*), (5.69, *2.53*), (*4.01*, 2.69) and (**3.58**, **1.93**). (b) shows the median ATE_t in City03 as a function of the number of LiDARs for the FULL and RAW.

79ms fully supporting 10 Hz. Further improvement is possible by performing downsampling before the undistortion if needed.

2) Accuracy: The impact of the number of LiDAR on accuracy is further evaluated using three datasets: TST, Whampoa, and City03. Comparing results with RAW in City03, error decreases as the number of LiDAR increases, with the error range also showing a reduction when examining the interquartile range and standard deviation in Fig. 10.

Notably, a significant error reduction is observed when increasing the number of LiDAR from one to two, while a minor reduction is seen when increasing from two to three (Fig. 10(a)). We speculate this is because an increment to two LiDARs provides sufficient constraint. Furthermore, as can be seen in the table in Fig. 10(b), it could be a fallacy to posit more LiDARs necessarily improve the performance. In City03, adding the second (Avia) and third (Tele) LiDARs do not effectively reduce error due to their narrow FOV and wide overlap with Ouster LiDAR. It emphasizes the importance of thoughtful LiDAR placement in multi-LiDAR systems. Moreover, using two LiDARs with FULL outperforms using three LiDARs with RAW. Merely merging point clouds in overlapping areas may not result in significant performance improvements. Instead, by employing B-spline interpolation to accurately transform points and assign uncertainty, FULL with three LiDARs gives the best performance.

IV. CONCLUSION

In this letter, we proposed a framework for asynchronous multiple LiDAR-inertial systems. The proposed framework utilizes B-spline interpolation in conjunction with an IMU discrete model to mitigate the temporal discrepancy among multiple LiDARs. To mitigate the accumulation of ambiguity during frame changes, a common issue in temporal compensation methods,

we proposed a method for propagating point-wise uncertainty based on IMU acquisition time and point distance from sensors. Additionally, we incorporated a localization weight to improve performance in challenging environments. Our method was validated through extensive experimentation on both public datasets and our dataset and achieved real-time performance while surpassing the state-of-the-art in terms of accuracy and robustness.

REFERENCES

[1] J. Jiao, H. Ye, Y. Zhu, and M. Liu, "Robust odometry and mapping for multi-LiDAR systems with online extrinsic calibration," *IEEE Trans. Robot.*, vol. 38, no. 1, pp. 351–371, Feb. 2022.

[2] M. Helmberger, K. Morin, B. Berner, N. Kumar, G. Cioffi, and D. Scaramuzza, "The hilti SLAM challenge dataset," *IEEE Robot. Automat. Lett.*, vol. 7, no. 3, pp. 7518–7525, Jul. 2022.

[3] L. Hsu et al., "UrbanNav: An open-sourced multisensory dataset for benchmarking positioning algorithms designed for urban areas," in *Proc. 34th Int. Tech. Meeting Satell. Division Inst. Navigation*, 2021, pp. 226–256.

[4] T.-M. Nguyen, S. Yuan, M. Cao, Y. Lyu, T. H. Nguyen, and L. Xie, "NTU VIRAL: A visual-inertial-ranging-lidar dataset, from an aerial vehicle viewpoint," *Int. J. Robot. Res.*, vol. 41, no. 3, pp. 270–280, 2022.

[5] A. Reinke et al., "LOCUS 2.0: Robust and computationally efficient LiDAR odometry for real-time 3D mapping," *IEEE Robot. Automat. Lett.*, vol. 7, no. 4, pp. 9043–9050, Oct. 2022.

[6] M. Palieri et al., "LOCUS: A multi-sensor lidar-centric solution for high-precision odometry and 3D mapping in real-time," *IEEE Robot. Automat. Lett.*, vol. 6, no. 2, pp. 421–428, Apr. 2021.

[7] J. Lin, X. Liu, and F. Zhang, "A decentralized framework for simultaneous calibration, localization and mapping with multiple LiDARs," in *Proc. IEEE/RSJ Intl. Conf. Intell. Robots Sys.*, 2020, pp. 4870–4877.

[8] T. Nguyen, S. Yuan, M. Cao, L. Yang, T. Nguyen, and L. Xie, "MILIOM: Tightly coupled multi-input LiDAR-inertia odometry and mapping," *IEEE Robot. Automat. Lett.*, vol. 6, no. 3, pp. 5573–5580, Jul. 2021.

[9] Y. Wang, W. Song, Y. Lou, F. Huang, Z. Tu, and S. Zhang, "Simultaneous localization of rail vehicles and mapping of environment with multiple LiDARs," *IEEE Robot. Automat. Lett.*, vol. 7, no. 3, pp. 8186–8193, Jul. 2022.

[10] J. Lv, K. Hu, J. Xu, Y. Liu, X. Ma, and X. Zuo, "CLINS: Continuous-time trajectory estimation for LiDAR-inertial system," in *Proc. IEEE/RSJ Int. Conf. Intell. Robots Sys.*, 2021, pp. 6657–6663.

[11] E. Mueggler, G. Gallego, H. Rebecq, and D. Scaramuzza, "Continuous-time visual-inertial odometry for event cameras," *IEEE Trans. Robot.*, vol. 34, no. 6, pp. 1425–1440, Dec. 2018.

[12] D. Feng, L. Rosenbaum, and K. Dietmayer, "Towards safe autonomous driving: Capture uncertainty in the deep neural network for lidar 3D vehicle detection," in *Proc. IEEE Intell. Transport. Sys. Conf.*, 2018, pp. 3266–3273.

[13] G. P. Meyer and N. Thakurdesai, "Learning an uncertainty-aware object detector for autonomous driving," in *Proc. IEEE/RSJ Int. Conf. Intell. Robots Syst.*, 2020, pp. 10521–10527.

[14] Y. Jung, M. Jeon, C. Kim, S. Seo, and S. Kim, "Uncertainty-aware fast curb detection using convolutional networks in point clouds," in *Proc. IEEE Intl. Conf. Robot. Automat.*, 2021, pp. 12882–12888.

[15] J. Jiao, P. Yun, L. Tai, and M. Liu, "MLOD: Awareness of extrinsic perturbation in multi-LiDAR 3D object detection for autonomous driving," in *Proc. IEEE/RSJ Intl. Conf. Intell. Robots Sys.*, 2020, pp. 10556–10563.

[16] T. Barfoot and P. Furgale, "Associating uncertainty with three-dimensional poses for use in estimation problems," *IEEE Trans. Robot.*, vol. 30, no. 3, pp. 679–693, Jun. 2014.

[17] B. Jiang and S. Shen, "A LiDAR-inertial odometry with principled uncertainty modeling," in *Proc. IEEE/RSJ Intl. Conf. Intell. Robots Sys.*, 2022, pp. 13292–13299.

[18] W. Xu, Y. Cai, D. He, J. Lin, and F. Zhang, "FAST-LIO2: Fast direct LiDAR-inertial odometry," *IEEE Trans. Robot.*, vol. 38, no. 4, pp. 2053–2073, Aug. 2022.

[19] W. Xu and F. Zhang, "FAST-LIO: A fast, robust LiDAR-inertial odometry package by tightly-coupled iterated Kalman filter," *IEEE Robot. Automat. Lett.*, vol. 6, no. 2, pp. 3317–3324, Apr. 2021.

[20] M. Grupp, "Evo: Python package for the evaluation of odometry and SLAM," 2017. [Online]. Available: https://github.com/MichaelGrupp/evo